Influence of geologic layering on heat transport and storage in an aquifer thermal energy storage system

D. W. Bridger · D. M. Allen

Abstract A modeling study was carried out to evaluate the influence of aquifer heterogeneity, as represented by geologic layering, on heat transport and storage in an aquifer thermal energy storage (ATES) system in Agassiz, British Columbia, Canada. Two 3D heat transport models were developed and calibrated using the flow and heat transport code FEFLOW including: a "non-layered" model domain with homogeneous hydraulic and thermal properties; and, a "layered" model domain with variable hydraulic and thermal properties assigned to discrete geological units to represent aquifer heterogeneity. The base model (non-layered) shows limited sensitivity for the ranges of all thermal and hydraulic properties expected at the site; the model is most sensitive to vertical anisotropy and hydraulic gradient. Simulated and observed temperatures within the wells reflect a combination of screen placement and layering, with inconsistencies largely explained by the lateral continuity of high permeability layers represented in the model. Simulation of heat injection, storage and recovery show preferential transport along high permeability layers, resulting in longitudinal plume distortion, and overall higher short-term storage efficiencies.

D. W. Bridger · D. M. Allen (✉)
Department of Earth Sciences, Simon Fraser University,
Burnaby, BC V5A 1S6, Canada
e-mail: dallen@sfu.ca

Present Address:
D. W. Bridger
SNC-Lavalin Inc. Environment Division,
Burnaby, BC V5A 4N6, Canada
e-mail: Dave.Bridger@snclavalin.com

Introduction

In response to an increased global demand for energy and growing environmental concerns over fossil fuel consumption and CO_2 emissions, there have been mounting efforts to conserve energy while employing existing technologies to reduce energy use by employing more energy-efficient technologies such as geothermal energy. Despite their benefits, a major limitation to the widespread use of these technologies especially in countries which undergo large seasonal temperature variations (i.e., temperate climates) is the presence of an imbalance between the supply and demand for energy. In order to resolve this imbalance, while attempting to reduce energy consumption, thermal energy storage may be employed.

Aquifer thermal energy storage (ATES) systems utilize low-temperature geothermal aquifer resources (e.g., Vanhoudt et al. 2011; Marx et al. 2011; Lee 2010; Bridger and Allen 2005, 2010; Bartels and Kabus 2003; Eggen and Vangsnes 2005; Paksoy et al. 2000; Hall and Raymond 1992; IF Technology 1995; Vail and Jenne 1994). The requirement for groundwater at different temperatures on a seasonal basis makes it desirable to use the heated or chilled water that is generated in the alternate (off-peak) season or period of low demand. The idea is that one does not "waste" the energy, but undertakes to "store" the energy in a suitable storage reservoir. If waste heat is added (returned) to groundwater when there is a cooling load in the summer season, then this waste heat can be potentially stored for use in the winter. The increase in temperature of the groundwater afforded by the injection of waste heat during the summer implies that the thermal store will be at a higher temperature than the ambient groundwater. The following heating season will then have a higher available supply temperature and an overall decrease in the amount of energy required for heating. Thus, ATES, in its simplest form, involves heating or chilling groundwater using low-grade

thermal energy such as solar heat or cold outside air temperatures, and injecting it into a suitable aquifer (Andersson 2007) for storage during periods of low demand. During periods of high demand, this water is extracted and its energy can be used for a variety of applications including space heating, greenhouse heating, air conditioning, industrial process cooling, and road de-icing.

In an ATES system, both conductive and convective transport occur due to the movement of the groundwater between wells and the temperature gradients that are induced from the stored water coming into contact with the surrounding aquifer water. Consideration of the distribution of hydraulic and thermal properties and the driving forces is necessary for designing the ATES system and for quantifying the rate of heat movement and storage capacity of the aquifer (e.g. Lee 2011; Kim et al. 2010; Andersson 2007; Bridger and Allen 2005). Aquifer heterogeneity has been shown as a key factor influencing thermal plume movement and energy recovery in ATES systems (Hidalgo et al. 2009; Bridger and Allen 2010; Xue et al. 1990; Busheck et al. 1983; Molz et al. 1983a, 1983b; Tsang et al. 1981). However, heterogeneous aquifers are difficult to characterize (both hydraulically and thermally), over relatively small scales (i.e., 10s to 100s of meters). Hydrogeologists are typically limited by the existing field methods and/or the high costs required for such detailed investigations.

The purpose of this paper is to investigate the influence of aquifer heterogeneity, as represented by geologic layering, on thermal energy transport and storage in an ATES system using a numerical modeling approach. Simulations are carried out to compare heat transport based on two conceptual models: a non-layered versus a layered system. The ATES system (described in the following section) was described by Bridger and Allen (2010). The authors discussed the drilling and aquifer testing program, analysed the suite of temperature logs that were collected prior to and during operation of the system, simulated groundwater flow and heat transport in the system during the first 2 years of operation, and compared the results to the observed temperatures. The role of heterogeneity was discussed only briefly. Therefore, the objective of this paper is to evaluate the effects of layered heterogeneity on thermal energy transport, storage, and recoverability.

The study site

The case study ATES system is located at the Agriculture and Agri-Foods Canada laboratory facility, also known as the Pacific Agricultural Research Centre (PARC), in Agassiz, British Columbia, Canada (Fig. 1). The system began operation in 2001, and provides both heating (with the aid of a heat pump) and cooling to the PARC facility, which comprises laboratory, office, industrial and greenhouse space (total 7,000 m^2). The estimated peak cooling capacity of the ATES system is 160 t (563 kW) and the total heating capacity is approximately 1,000 MBtu/h (293 kW) (Maynard, Agriculture Canada 2006).

The well field comprises four 60-m deep production wells spaced 90 m apart, with two wells used to store warm energy (WW2 and WW4) and two wells used to store cold energy (CW1 and CW3) (Fig. 1). An additional well, called the "dump well", was installed down-gradient from the active well field to a depth of 36 m to allow for dissipation of heat during peak cooling periods in the summer months. Three monitoring wells (MW1, MW2, MW3) were installed to 60 m depth, at one third and two thirds distances from the production wells, and one monitoring well (MW4) was installed to the northeast of the dump well (Fig. 1).
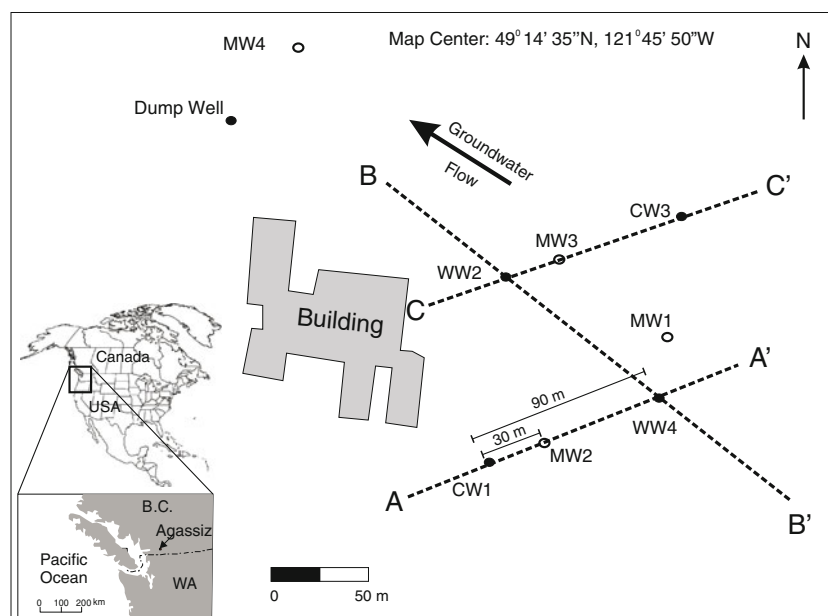

Fig. 1 Site map of the Pacific Agricultural Research Centre (PARC) in Agassiz, British Columbia (*BC*), Canada. Shown is the building footprint, the five production wells (warm wells *WW2* and *WW4*, cold wells *CW1* and *CW3*, and one dump well), and four monitoring wells (*MW1–4*). Also shown are the lines of cross-section used to display temperature results in Figs. 8, 9, 11, 13 and 15. *WA* is Washington State

The aquifer at the site is heterogeneous in nature and comprises a 100-m-thick sequence of stratified sands and gravels of fluvial origin (Fig. 2). Higher permeability layers of coarse sands and gravels identified within the aquifer present an operational concern for the Agassiz ATES system due to the potential for hydraulic (and thermal) short-circuiting between production wells. Therefore, the production wells were screened with multiple screens; blank sections (i.e. no screen) were placed over intervals that were thought to potentially act as short-circuit layers. Despite placement of multiple well screens in each well to avoid these high permeability layers (Fig. 2), the temperature logs collected from the well field during the first year of system operation indicated that some thermal short-circuiting had occurred after 7 months of cooling (Bridger and Allen 2010).

Methodology

Model construction

The scope of modeling included the development of both a "non-layered" 3D model of the study site with homogeneous hydraulic and thermal properties, and a "layered" 3D model of the study site with variable hydraulic and thermal properties assigned to discrete layers to represent aquifer heterogeneity. Simulation results from the two models are compared to evaluate the effects of aquifer heterogeneity on heat transport (as thermal plume extent/configuration) and storage (as energy recoverability). Model development included flow calibration/verification to steady-state hydraulic heads and observed pumping test drawdowns, and an evaluation of model sensitivity to aquifer and flow and heat transport properties.

As model development was discussed in detail by Bridger and Allen (2010), only a brief summary is given here. The code FEFLOW v. 5.2 (WASY 2005) was used for the simulations. FEFLOW is able to incorporate spatially variable aquifer properties, geologic layering, and screening of pumping/injection wells over multiple intervals, making it well suited for simulating the Agassiz system. Fluid density and viscosity variations resulting from the injection of higher temperature (15 °C) and lower temperature (6–7 °C) water into the aquifer were not accounted for in the simulations due to the small differences in density of water expected at these temperatures—e.g., density of water ranges from 0.999943 g/L at 6 °C to 0.999102 g/L at 15 °C, based on the calculation method of Fofonoff and Millard (1983)—and the potential for rapid advection at the site, which will minimize buoyancy-related convective flow.

The same 3D model domain was used for the non-layered and layered models (Fig. 3). The domain extends 640 m × 720 m in the x and y dimensions, respectively, and extends a distance of 100 m in the vertical direction (z-dimension).
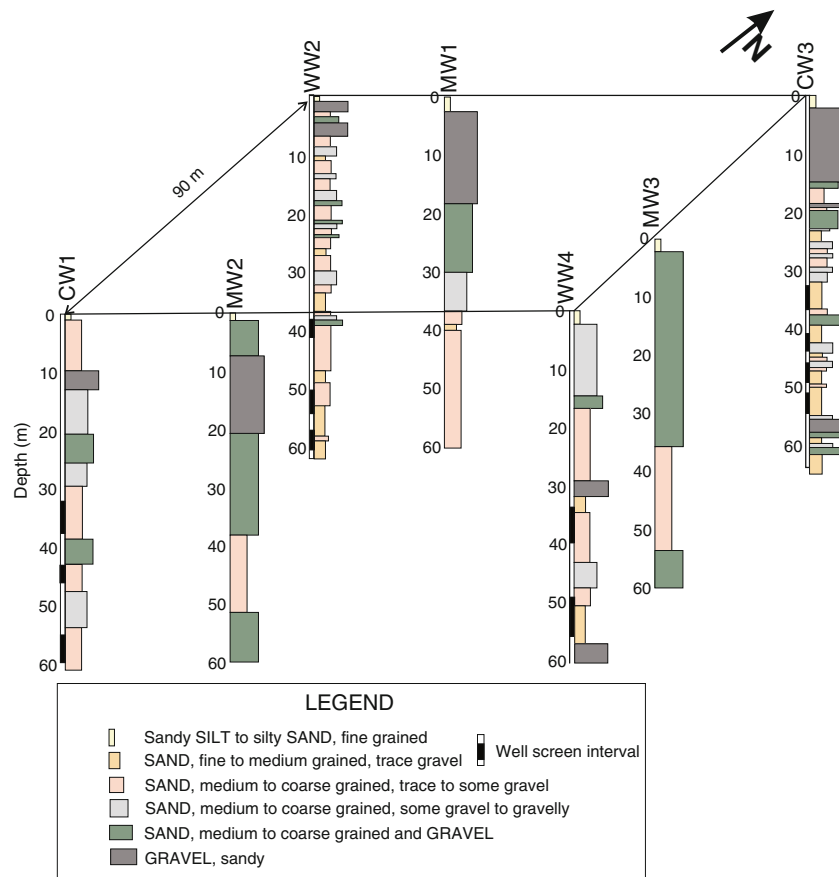

Fig. 2 Borehole stratigraphy in the well field. The locations of screened intervals in the production wells are shown (modified from Bridger and Allen 2010)
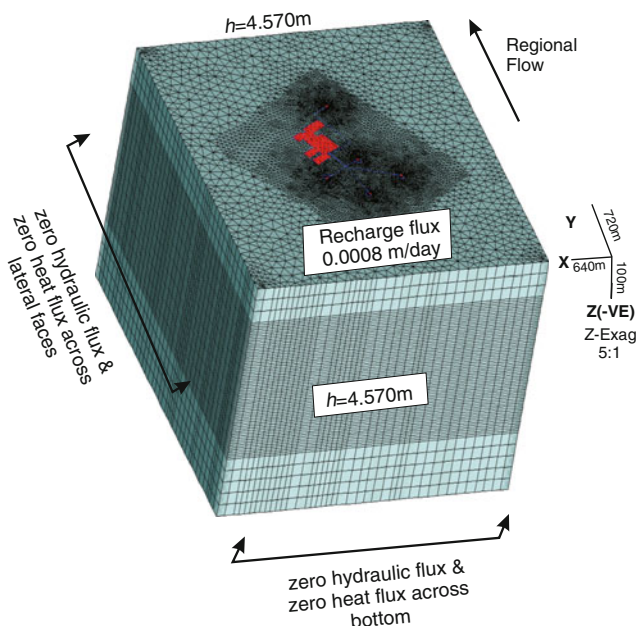
Fig. 3 The model grid showing the boundary conditions applied to the model

Lateral element dimensions range from 10 m at the domain outer boundaries to 1 m adjacent to the production/injection wells. The domain is discretized into 68 horizontal layers with layer spacing of 1 m between 15 and 75 m depth, and 5 m layer spacing above and below. Closer layer spacing was used for the region expected to experience the most significant hydraulic and thermal effects. The domain is rotated to align the y-axis parallel to the inferred direction of groundwater flow (see Fig. 1). Observation points were input at the production and monitoring well locations at 1-m intervals to allow tracking of hydraulic head and temperature during the simulations.

The same hydraulic and temperature boundary conditions were assigned to each model domain (Fig. 3). Boundary conditions are invariant in time and aim to represent typical conditions at the site. Specified (constant) hydraulic head values of −4.102 and −4.570 m were assigned over the entire vertical faces of the upgradient and downgradient lateral boundaries (720 m distance in y-axis direction), respectively, corresponding with the observed hydraulic gradient (0.00065 m/m) and water-table depth (approximately 4.3 m) in the vicinity of the well-field. Zero flux (no flow) conditions were assigned along the lateral boundaries of the domain oriented perpendicular to the inferred groundwater flow direction and along the bottom boundary of the domain. A specified flux of 0.0008 m/day was applied to the top surface of the model domain to account for recharge. This recharge value was reported previously by Golder Associates Ltd. (unpublished report, 1998) and corresponds to approximately 19 % of mean annual precipitation for the site. Ambient groundwater temperatures (9.2–9.4 °C) are observed below 30 m depth within the screened portion of the aquifer. Effects within this zone from ground-surface-temperature variations and/or increasing temperatures with depth due to the

geothermal gradient were not observed and, therefore, zero heat-flux boundary conditions were assumed for the top and bottom surfaces of the model domain. A zero heat flux condition was assumed for the lateral boundaries of the domain, based on the large size of the model domain relative to thermal plume sizes (i.e., thermal plumes not expected to impact model boundaries).

The aquifer hydraulic and thermal properties used as input to the model are presented in Table 1. The values shown for each property represent an average based on field measurement of the parameter or from the literature as described in the following. Values are grouped into different stratigraphic units based on the relative proportions of silt, sand and gravel determined from grain-size analysis curves and drilling log descriptions. This level of detail was required for assigning aquifer hydraulic and thermal properties to the individual layers of the more complex three-dimensional (3D) layered domain, discussed in the following.

Values of hydraulic conductivity (K) shown in Table 1 were derived using the method of Hazen (1893) from grain-size analysis results of over 60 soil samples collected during the drilling of production wells—a detailed description of the methodology used for deriving K values from grain size results can be found in Bridger (2006). Values for specific storage (Ss) and specific yield (Sy) were based on the average of a range of literature values for similar geologic materials. These properties were grouped into only three stratigraphic units (i.e., units 2, 3, and 4 combined to form a single unit for sand) as literature values were not available for each unit as described in Table 1.

Values of heat capacity (C_{solid}) and thermal conductivity (k_{solid}) for the solid matrix (Table 1) are based on values for dry sand and gravel reported by Hellstrom and Sanner (2000). Aquifer heat capacity and thermal conductivity estimates were calculated from the assumed values of porosity (n) and solid thermal conductivity and solid heat capacity (equations following Table 1). The calculated values of aquifer heat capacity and aquifer thermal conductivity are consistent with reported values for similar geologic materials (Witte et al. 2002; Palmer et al. 1992; Hellstrom and Sanner 2000). Longitudinal (α_L) and transverse (α_T) dispersivities were set to 5.0 and 0.5 m, respectively. FEFLOW does not incorporate the two components of transverse dispersivity, namely horizontal (α_{TH}) and transverse (α_{TV}) dispersivity. This is an important limitation of the code because typically $\alpha_{TV} < \alpha_{TH}$ by at least an order of magnitude (Anderson and Woessner 1992). The effect on the model simulation results would be more dispersion in the vertical direction than might actually occur. The values used for these two parameters were the default values in FEFLOW, which have been used in other studies for sites of similar size (Lo Russo and Vincenzo Civita 2009). Typical dispersivity values used for simulating transport (solute and heat) for domains with similar spatial dimensions (perhaps slightly larger) are 10.0 and 0.1 m, respectively (Anderson and Woessner 1992). However, given the uncertainty in these parameters, the model sensitivity to dispersivity was evaluated as discussed in the following.

For the non-layered model domain, the average property values shown for unit 4 (gravelly sand) were uniformly

Table 1 Input values for aquifer hydraulic and thermal properties for each unit in the layered model. For the non-layered model, the values for unit 4 were applied to the full domain (modified from Bridger and Allen 2010)

Unit	Description[a]	Hydraulic properties			Thermal properties				
		K (10^{-4} m/s)[b]	Ss (10^{-5} 1/m)[c]	Sy[d]	n[e]	C_{solid}[f] ($\times 10^6$ J/m³/K)	k_{solid}[f] (J/m s K)	C_{aquifer}[g] ($\times 10^6$ J/m³/K)	k_{aquifer}[h] (J/m s K)
1	Sandy SILT to silty SAND, fine grained	0.016	30	0.21	0.42	1.60	0.40	2.69	2.54
2	SAND, fine to medium grained, trace gravel	2.0	9.6	0.29	0.38	1.40	0.40	2.38	2.67
3	SAND, medium to coarse grained, trace to some gravel	6.0	9.6	0.28	–	–	–	–	–
4	SAND, medium to coarse grained, some gravel to gravelly	9.2	2.2	0.25	0.32	1.50	0.40	2.35	2.74
5	SAND, medium to coarse grained and gravel	29	2.2	0.25	–	–	–	–	–
6	Gravel, sandy	71	2.9	0.24	–	–	–	–	–

[a] Secondary grain sizes based on following criteria: 'trace' 0–10 %, 'some' 10–20 %, 'y/ly/ey' 20–35 %, 'and' 35–50 %

[b] Values obtained from grain-size analysis results using method of Hazen (1893)

[c] Values reported by Baker and Pavlik (1990); Jumikis (1962); Domenico (1972); Rehm et al. (1980); Akindunni and Gillham (1992)

[d] Values reported by Anderson and Woessner (1992); Johnson (1967); Morris and Johnson (1967)

[e] Values from Davis (1969); Morris and Johnson (1967)

[f] Values from Hellstrom and Sanner (2000)

[g] Aquifer heat capacity (c_{aquifer}) calculated using equation: $c_{\text{aquifer}} = c_{\text{fluid}} \times n + (1-n)c_{\text{solid}}$

[h] Aquifer thermal conductivity (k_{aquifer}) calculated using equation: $k_{\text{aquifer}} = k_{\text{fluid}}{}^{n} + k_{\text{solid}}{}^{(1-n)}$

assigned as initial values for model calibration (Table 1). The values assigned for hydraulic properties ($K = 9.2 \times 10^{-4}$ m/s, Ss = 2.2×10^{-5} 1/m, Sy = 0.25) were within the ranges of values reported for the pumping test conducted at WW2 (Golder Associates Ltd., unpublished report, 1998). A horizontal-to-vertical conductivity anisotropy ratio ($K_{xy}:K_z$) of 10:1 was assumed for the non-layered domain to account for stratification and observed layering within the aquifer. This anisotropy ratio was assumed to be reasonable based on literature values from similar geologic materials (Freeze and Cherry 1979; Moench et al. 2001).

For the layered domain, aquifer property values were assigned to each model layer (1 m spacing) at all five production wells, based on the observed stratigraphic descriptions (Table 1). The values were then imported into FEFLOW and interpolated using kriging. Kriging, like any interpolation method, has its limitations. However, this method does honour the available data points and does not tend to create "bulls eyes", which are common in inverse distance methods. It is important to note that hydraulic conductivity values for the monitoring wells were excluded from data contouring due to the poor resolution of geologic layers within the drilling logs. A more rigorous geostatistical analysis could be done had the dataset offered more points. The results of contouring of hydraulic conductivity values are shown in Fig. 4a for the 3D model domain. As shown in Fig. 4b, a few 'control points' with K values similar to the measured ones were added within of the well-field area, and uniform values were added around the periphery of the well field and at the model domain edges in order to constrain the contouring.

For both the non-layered and layered models, multiple well screens in the production wells were incorporated. Pumping well boundary nodes were applied to the finite element nodes and layers corresponding both to the depths and screen interval lengths of the production wells. The total pumping (or injection) rates for each screen were proportioned on the basis of screen length for the non-layered FEFLOW domain, and both screen length and K for the layered FEFLOW domain. An example of the proportioned pumping rates for production well WW2 for both the non-layered and layered model domains is shown in Table 2. The injected water is introduced in the operating system via a vertical drop pipe positioned at the top of the well, several meters below the water table. This allows for thorough mixing along the borehole and results in an isothermal water column as evidenced by the temperature logs obtained during injection. Because FEFLOW does not have a second type flow boundary condition (flux) that can be assigned a particular injection temperature, the injection of cold and warm water into the aquifer was simulated by assigning a constant temperature boundary condition along the well location for all layers corresponding with well screens. This is a current limitation of FEFLOW and the approach may result in less mixing between the injected water and aquifer water in the near vicinity of the borehole. However, the observed isothermal conditions indicate that a fixed temperature boundary condition is a reasonable approximation. During pumping, groundwater simulated temperatures were recorded for each well screen.

Results

Flow calibration

Flow calibration of the non-layered and layered models included obtaining a match to the observed background flow field (prior to pumping) and transient calibration to
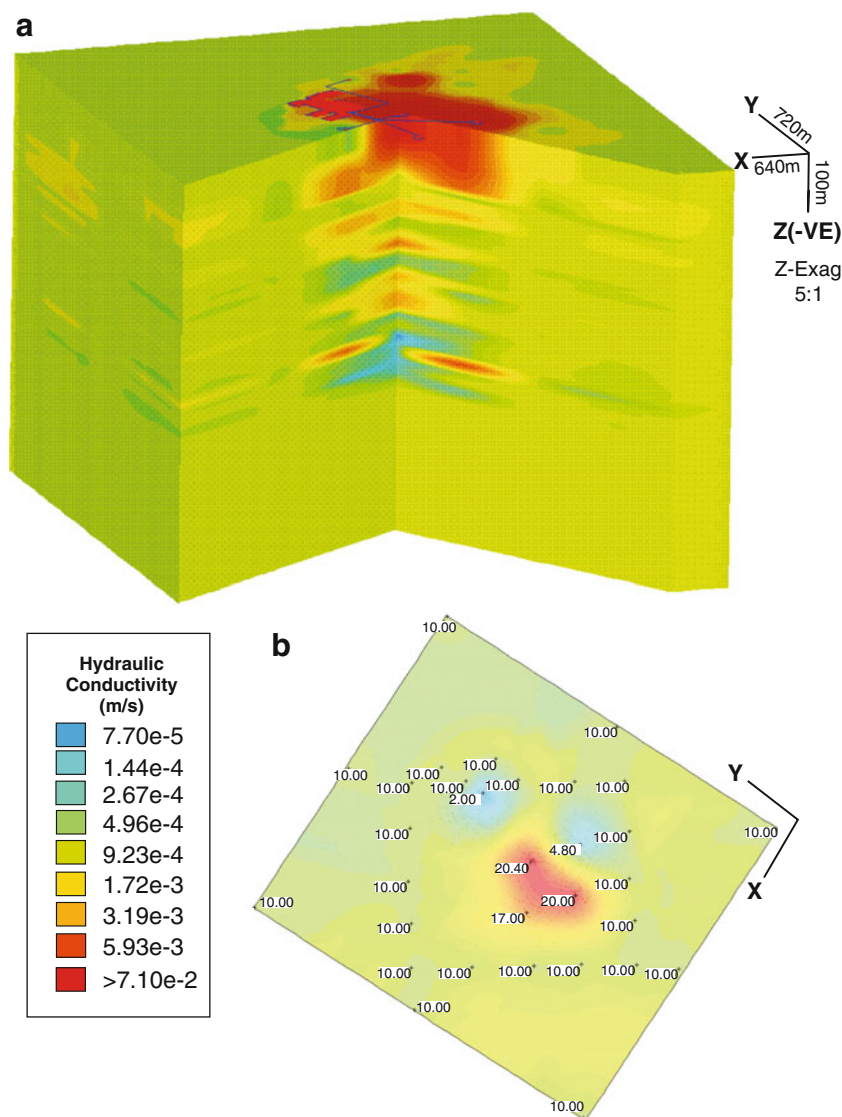
Fig. 4 **a** Cut-away through the layered model domain showing the hydraulic conductivity variation. **b** Slice through the model domain (layer 31 at 42 m depth) showing the resulting hydraulic conductivity distribution and the control points used to constrain the interpolation

observed drawdowns from a constant discharge pumping test conducted in production well WW2. Steady-state model calibration to the observed flow direction and hydraulic gradient (0.00065 m/m) in the well field was easily achieved for the non-layered and layered model domains. Simulated depths to the water table in the well field ranged from 4.28 to 4.33 m, which are generally consistent with water levels observed in production wells and monitoring wells (~4.2 m depth).

Transient model calibration involved simulating the pumping test at WW2 for each domain. This well was pumped at a constant rate of 2,475 m³/day (454 US gpm) for a period of 2,700 min (45 h) and water-level drawdowns were monitored in CW3 and MW4, located at distances of 96 and 156 m, respectively, from the pumping well (see Fig. 1). At the time of this pumping test, these were the only wells available at the site; WW4, CW1, and MW1, MW2,

and MW3 had not yet been drilled. Simulation results were compared only to the first 1,100 min (18.3 h) of the test due to the occurrence of interference effects beyond this time, which were inferred to be from either pumping of nearby wells or variability in the pumping rate of the test pump (Golder Associates Ltd., unpublished report, 1998). Observed drawdown data from the pumping well were corrected for well losses based on the average well efficiency (75 %) determined from step tests conducted at WW2.

Simulated drawdown curves for the entire well (in order to compare with measured drawdown in the well) were obtained by averaging the computed drawdown for each individual well screen in each well. The drawdown for each single well screen section was obtained by subtracting the simulated head from initial hydraulic head at each 1 m layer corresponding to a particular well screen, and then averaging the resulting drawdowns obtained from all of the model

Table 2 Proportioning of total pumping rate for multiple well screens in WW2 (from Bridger and Allen 2010)

Screen No.	Screen depth (m)	Screen length (m)	% Screen length	Non-layered domain Flow rate (m³/day)	Layered domain Average K^a (m/s)	% Screen length[b]	Flow rate (m³/day)
1	33.2–36.2	3.0	23.1	571.1	4.1×10^{-4}	13.4	331.4
2	38.1–41.1	3.0	23.1	571.1	2.0×10^{-3}	66.4	1,643.4
3	50.2–54.2	4.0	30.8	761.5	3.5×10^{-4}	15.3	378.8
4	57.2–60.2	3.0	23.1	571.1	1.5×10^{-4}	4.9	121.2
	Total	13.0	100	2,474.8		100	2,474.8

[a] Average K obtained based on average of Hazen K values from grain-size results within screened interval

[b] % Screen length for *Layered domain* calculated by multiplying the length of screen section by the average hydraulic conductivity value within the screen section divided by the total length

layers corresponding to that well screen. Calibration involved adjusting values of horizontal hydraulic conductivity, vertical hydraulic conductivity, specific storage, and specific yield to improve the fit between simulated and observed drawdown curves in the pumping well (corrected for well losses) and observation wells (calibration details are provided in Bridger (2006) along with the results of a sensitivity analysis undertaken to determine the sensitivity of the drawdown curves to variation in these parameters). Figure 5 shows a plot of simulated and observed drawdown for the pumping well (WW2) and the observation wells CW3 and MW4 for both the non-layered and layered domains. For both domains, a good match to observed conditions was obtained for both the height and shape of the simulated drawdown curves in all three wells. The values of aquifer flow properties used to obtain the best fit or calibrated results for each simulation domain are shown in Table 3, along with the simulation results reported as percentage root mean squared error (RMS) for each of the wells, and an overall average for each of the modeling approaches.

Overall, the results of transient calibration to the pumping test indicate that the incorporation of discrete layering in the layered domain does not appear to provide any significant advantage for simulating hydraulic response of the aquifer to pumping. This is based on the reasonable match to observed drawdown curves achieved for both models. The influence of layering on the hydraulic response of the aquifer to pumping, however, is evident from slight variations in the drawdown curves obtained from the different screen intervals in each well (see Bridger 2006). These effects are more apparent when heat is considered as discussed in the following.

Heat transport simulations

The heat transport simulations included: (1) a sensitivity analysis to evaluate the model sensitivity to ranges in thermal and hydraulic aquifer properties expected at the site; and (2) a comparison of simulated thermal energy transport, storage, and recovery in the non-layered and layered model domains.

Sensitivity analysis

The overall objective of the sensitivity analysis was to attempt to quantify and develop an improved understanding of uncertainty in the thermal and aquifer properties on heat transport in the Agassiz model. The sensitivity analysis was
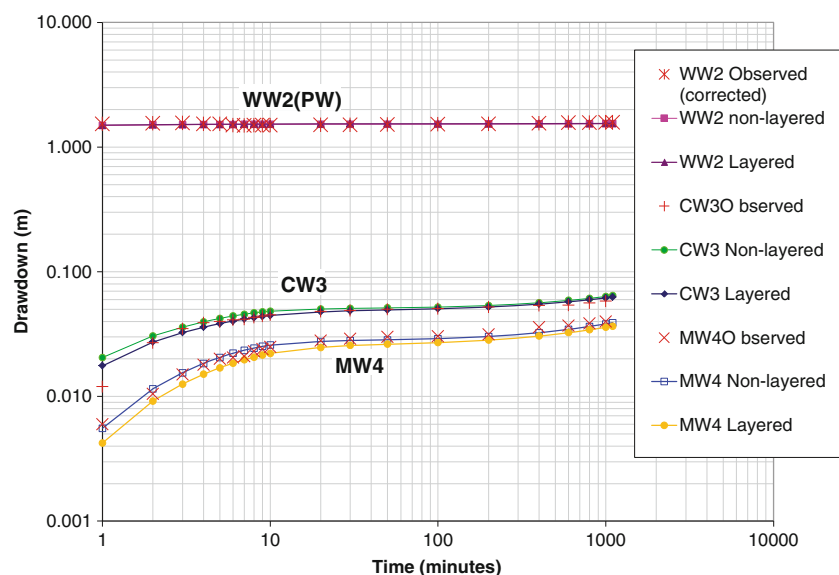

Fig. 5 Observed drawdown in WW2, CW3 and MW4 and simulated drawdown for each of the non-layered and layered domains (modified from Bridger and Allen 2010)

Table 3 Flow calibration results for the non-layered and the layered domains as RMS error

"Best fit" model parameters	RMS error (%)			
	WW2	CW3	MW4	Overall
Non-layered domain:	30	8	5	15
Hydraulic conductivity, $K_{xy}=1.05\times10^{-3}$ m/s				
Vertical anisotropy, $K_{xy}/K_z=5.4{:}1$				
Specific storage, Ss$=1.0\times10^{-5}$ 1/m				
Specific yield, Sy$=0.2$				
Layered domain:	30	5	9	15
Variable K, Ss, Sy values				
Vertical anisotropy incorporated at $K_{xy}/K_z=10{:}1$				
Ss values decreased by factor of 0.2				
Control points with $K=1.0\times10^{-3}$ m/s introduced outside of well field to constrain contouring				
K increased in production wells by factor of 1.4				
Decreased K to 1.0×10^{-3} m/s in MW4 between 5 and 30 m depth				

carried out in the context of a single thermal energy injection scenario using the non-layered model. A complete sensitivity analysis using the layered model domain was not conducted due to the considerable effort required to set up each layered model run (i.e., create, assign, and contour 60 unique layers). Although performing the sensitivity analysis with the layered model would have been preferred as it more closely represents true system behaviour, use of the non-layered model was adequate for the objective defined in the preceding.

All parameters were varied within the range of uncertainty for the study site. Thermal and transport properties included aquifer heat capacity, aquifer thermal conductivity, and longitudinal and transverse dispersivities. Aquifer heat capacity and aquifer thermal conductivity were calculated from minimum and maximum values of porosity, dry soil heat capacity and thermal conductivity reported in the literature for the aquifer materials at the site (average values are given in Table 1). The base-case model values and ranges used for sensitivity are given in Table 4. Porosity was not evaluated directly, but was varied indirectly through the calculation of aquifer heat capacity and thermal conductivity to obtain maximum and minimum values of these properties. Hydraulic boundaries and properties included hydraulic gradient (dh/dl), hydraulic conductivity (K), and vertical anisotropy of hydraulic conductivity (K_{xy}/K_z). Although flow properties were already considered calibrated to the Agassiz aquifer conditions for both models, determining their relative influence on heat transport was important, both in the context of providing an investigation of all relevant variables and assessing the consequence of any uncertainty in the estimates obtained during the flow calibration. It is

important to note that the range of values attempted was not exhaustive (minimum and maximum ranges only) and represented, in most cases, plausible estimates of hydraulic and thermal properties that could occur in the study area.

The sensitivity analysis was performed using the non-layered model domain by individually assigning high and low values of each property, as shown in Table 4. Parameter values for the base case correspond to the values in Table 1 for unit 4, as used in the non-layered model. Injection of 14 °C water at a rate of 914.4 m³/day was carried out at WW4 for all sensitivity simulations with the same amount of water extracted from CW1. The injection temperature and well pumping/injection rate correspond roughly to the assumed operating conditions of the Agassiz ATES system at the beginning of the first cooling season in 2001. Results are interpreted temporally at one observation point, and spatially after 120 days of injection.

Monitoring well MW3 is situated closest to WW4; therefore, the temperatures at 44 m depth in this monitoring well (same depth interval as the injection interval) were used to explore the timing of thermal breakthrough. Figure 6a shows the results of the sensitivity analysis for thermal and transport properties, and Fig. 6b shows the results for hydraulic boundary condition and hydraulic properties. The model shows limited sensitivity for the ranges of thermal and hydraulic properties tested; simulated temperatures at MW3 are within 1 °C. The model is most sensitive to vertical anisotropy and hydraulic gradient (Fig. 6b). For the high hydraulic gradient, the temperatures at MW3 do not increase due to the development of an elongated plume from WW4; MW3 is situated outside the plume area (Fig. 7). Figure 7 compares in plan view (for a depth of 44 m) the temperature

Table 4 Ranges of hydraulic and thermal properties used in the heat transport sensitivity analysis

| Property	Base case	Range for sensitivity analysis
Hydraulic properties		
Hydraulic gradient (dh/dl)	0.001 m/m	0.0001–0.0065 m/m
Hydraulic conductivity (K_{xy})	9.2×10^{-4} m/s	8.0×10^{-4}–1.2×10^{-3} m/s
Anisotropy (K_{xy}/K_z)	5.4:1	1:1–10:1
Thermal properties		
Aquifer heat capacity ($C_{aquifer}$)	2.35×10^6 J/m³/K	2.03×10^6–2.90×10^6 J/m³/K
Aquifer thermal conductivity ($k_{aquifer}$)	2.74 J/m s K	1.96–3.57 J/m s K
Longitudinal dispersivity (α_L)	1.5 m	0.3–15 m
Transverse dispersivity (α_T)	0.15 m	0. 03–1.5 m
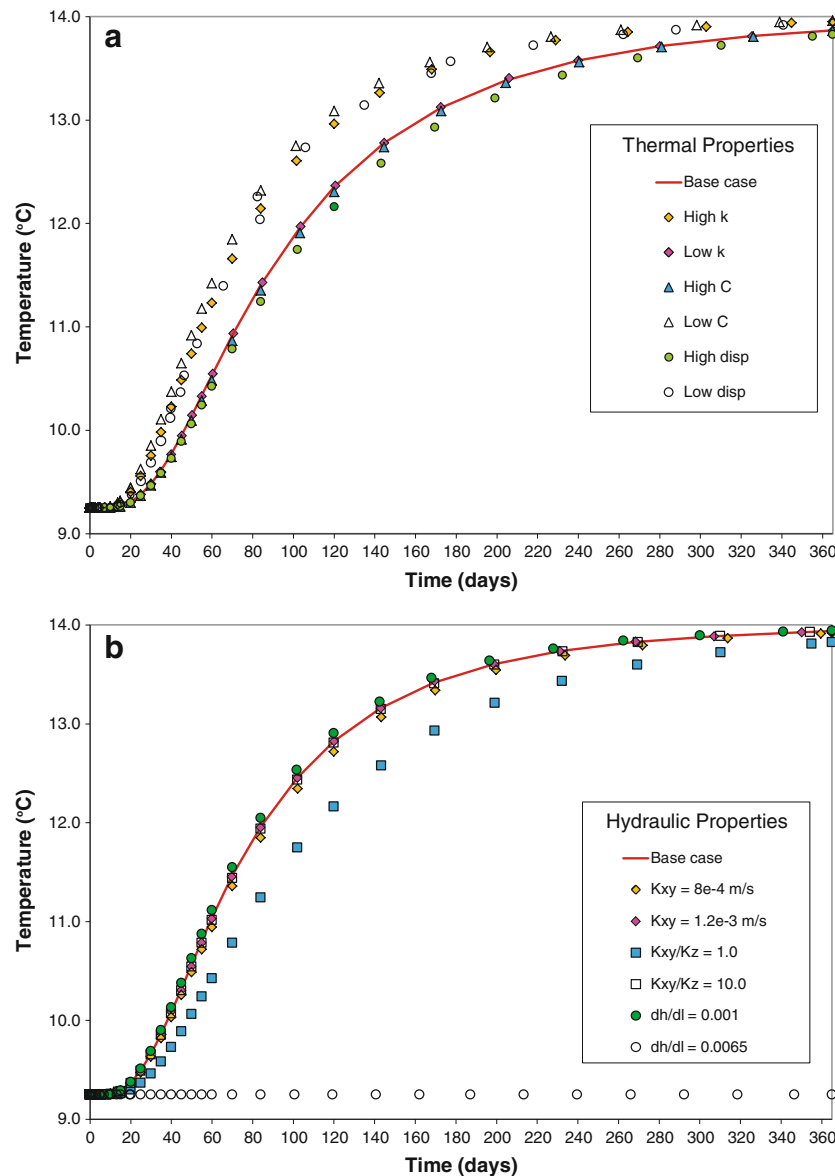
Fig. 6 Simulated temperature versus time at 44 m depth in MW3 during the sensitivity analysis for **a** ranges of thermal properties (k = thermal conductivity, C = heat capacity, disp = dispersivity) and **b** different hydraulic boundary conditions and ranges of hydraulic properties (K_{xy} = hydraulic conductivity, K_{xy}/K_z = anisotropy)

plumes for the base case, the case of high dispersivity, and the case for high hydraulic gradient.

Another way to compare variations in transport distance for the different thermal and hydraulic parameters considered in the sensitivity analysis is to measure plume dimensions. While perhaps not a rigorous statistical approach, plume dimensions can be informative for roughly estimating transport distances given parameter uncertainty. Temperature contours (similar to what are shown in Fig. 6) in plan view (layer by layer) and in cross-section from WW4 (injecting) to CW1 (pumping) were generated for each parameter, and the position of the 10 °C contour measured. Measurements included plume length (measured both from WW4 towards the pumping well at CW1 and from WW4 in

the direction of regional flow towards WW2), plume width (measured perpendicular to groundwater flow directions: down-gradient and towards pumping well) and plume vertical thickness. The results are summarized in Table 5 as percent increases (+) or decreases (−) in plume dimensions relative to the initial base case. The results are consistent with the results simulated at MW3, and indicate that with the exception of vertical anisotropy and hydraulic gradient, the model is generally insensitive to changes in parameters within the expected range for the site. This suggests that the level of flow calibration achieved in the model is adequate for accurately simulating heat transport (i.e., any further improvements in model calibration would not have a significant effect on heat transport).
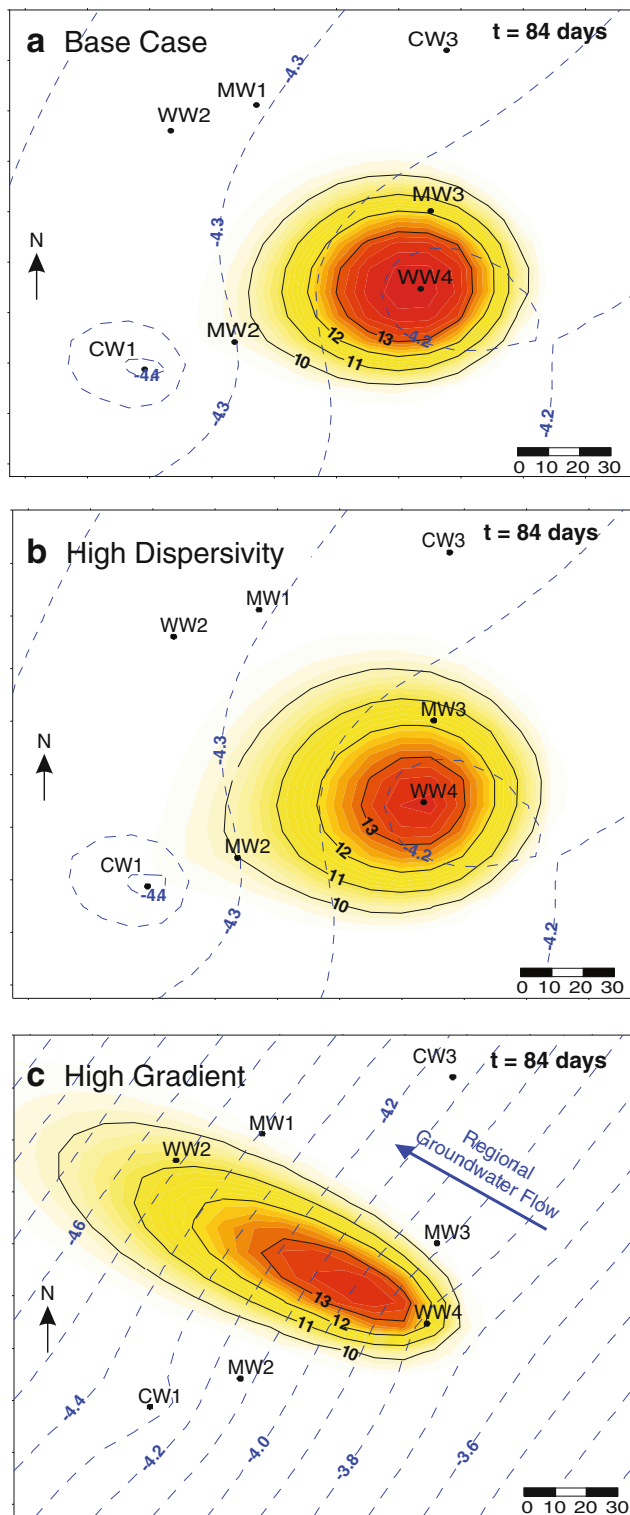
Fig. 7 Plan view of sensitivity analysis results at a depth of 44 m for **a** base case, **b** high dispersivity, and **c** high hydraulic gradient. Contours for hydraulic head (m) (*blue dashed*) and temperature (°C) (*solid black*) are shown

Effects of geologic layering

The effects of geologic layering were evaluated by comparing simulation results from both the non-layered and layered model domains during the thermal energy

injection, storage, and recovery phases of an ATES cycle. The simulations included: (1) simulating injection of 14 °C water at a rate of 914.4 m³/day into each of WW4 and WW2 (separate simulations); (2) storage of thermal energy in the aquifer for periods of up to 1 year; and (3) recovery of thermal energy from the aquifer, both immediately following injection (after 120 days) and after a typical storage period of 3 months. The injection temperature and respective pumping/injection rate correspond approximately with the assumed average operating conditions of the Agassiz ATES system during the first cooling season in 2001. Pumping/injection rates were determined by averaging the total volume of water extracted from or injected into each well over the course of the cooling season.

Injection results are shown in Fig. 8 for a cross-section extending through CW1 (pumping) and WW4 (injecting) for each of the non-layered and layered models at the end of the injection period at 120 days. The results clearly show the effects of layering on the thermal plume. The shape of the thermal plume in the layered domain is distorted and elongated in the horizontal direction, and is narrower with steeper temperature gradients at the top and bottom of the plume. In addition, the thermal plume is transported further in the layered domain during the same amount of time, as evidenced by thermal breakthrough at CW1 after 120 days.

Figure 9 shows the outline of the simulated thermal plume at WW4 after 84 days of injection overlaid on the contoured hydraulic conductivity distribution (black to grey shading) obtained from the model layers. Shown are cross-sections through CW1 (pumping), MW2 (monitoring) and WW4 (injecting) (A–A′), and through WW2 (not pumping) and WW4 (injecting) parallel to the direction of regional groundwater flow (B–B′). Higher permeability layers, which dominate the geology of the aquifer, are shown with a darker grey colour. The low permeability layers are shown in light grey. These plots show that heat moves preferentially through higher permeability layers in the aquifer, both under the influence of pumping and the regional groundwater flow. Heat transport appears to be greatest in the high permeability layer present between the upper and lower screens in WW4 (from 40 to 47 m depth). In Fig. 9a (CW1 to WW4), this high permeability layer thins out towards CW1 and passes through the well above the second screen at 43 m depth. In Fig. 9b (WW2–WW4), this layer is shown to extend to WW2.

To explore more closely the effect of heterogeneity on heat transport during this injection simulation, the simulation results are compared to observed temperatures monitored in the wells. Temperature logs were collected prior to system start-up and periodically thereafter during operation. Bridger and Allen (2010) explore the full suite of temperature logs in more detail, relating the results to one full year of operation of the ATES system. Here, selected logs are used to illustrate how the simulation results compare to the observed temperatures. An important caveat is that fluid may mix slightly up and down the production wells because these are screened only at discrete levels—the unscreened portions may short-circuit fluid up/down the water column—although this is not considered to be a major problem.

Table 5 Summary of heat transport sensitivity analysis results

Condition	Value	Plume length		Plume Width	Plume Thickness
		WW4 to CW1	WW4 to WW2		
Base condition	Calibrated model	54 m	54 m	36 m	52 m
Increased heat capacity, $C_{aquifer}$	2.90×10^6 J/m^3/K	−9 %	−7 %	−8 %	−2 %
Decreased heat capacity, $C_{aquifer}$	2.03×10^6 J/m^3/K	9 %	9 %	3 %	4 %
Increased thermal conductivity, $k_{aquifer}$	3.57 J/m s K	6 %	4 %	3 %	4 %
Decreased thermal conductivity, $k_{aquifer}$	1.96 J/m s K	−9 %	−7 %	−6 %	0 %
Increased dispersivities, α_L and α_T	15.0 and 1.5 m	17 %	13 %	11 %	12 %
Decreased dispersivities, α_L and α_T	0.3 and 0.03 m	−7 %	−4 %	−3 %	−2 %
Increased hydraulic conductivity, K_{xy}	1.2×10^{-3} m/s	2 %	4 %	0 %	2 %
Decreased hydraulic conductivity, K_{xy}	8.0×10^{-4} m/s	0 %	−4 %	−3 %	4 %
Increased vertical anisotropy, K_{xy}/K_z	10:1	2 %	2 %	3 %	−1 %
Decreased vertical anisotropy, K_{xy}/K_z	1:1	−17 %	−11 %	−17 %	46 %
Increased hydraulic gradient, dh/dl	0.0010 m/m	2 %	7 %	−11 %	2 %
Increased hydraulic gradient, dh/dl	0.0065 m/m	−43 %	152 %	−64 %	−25 %
Decreased hydraulic gradient, dh/dl	0.0001 m/m	−6 %	−11 %	22 %	6 %
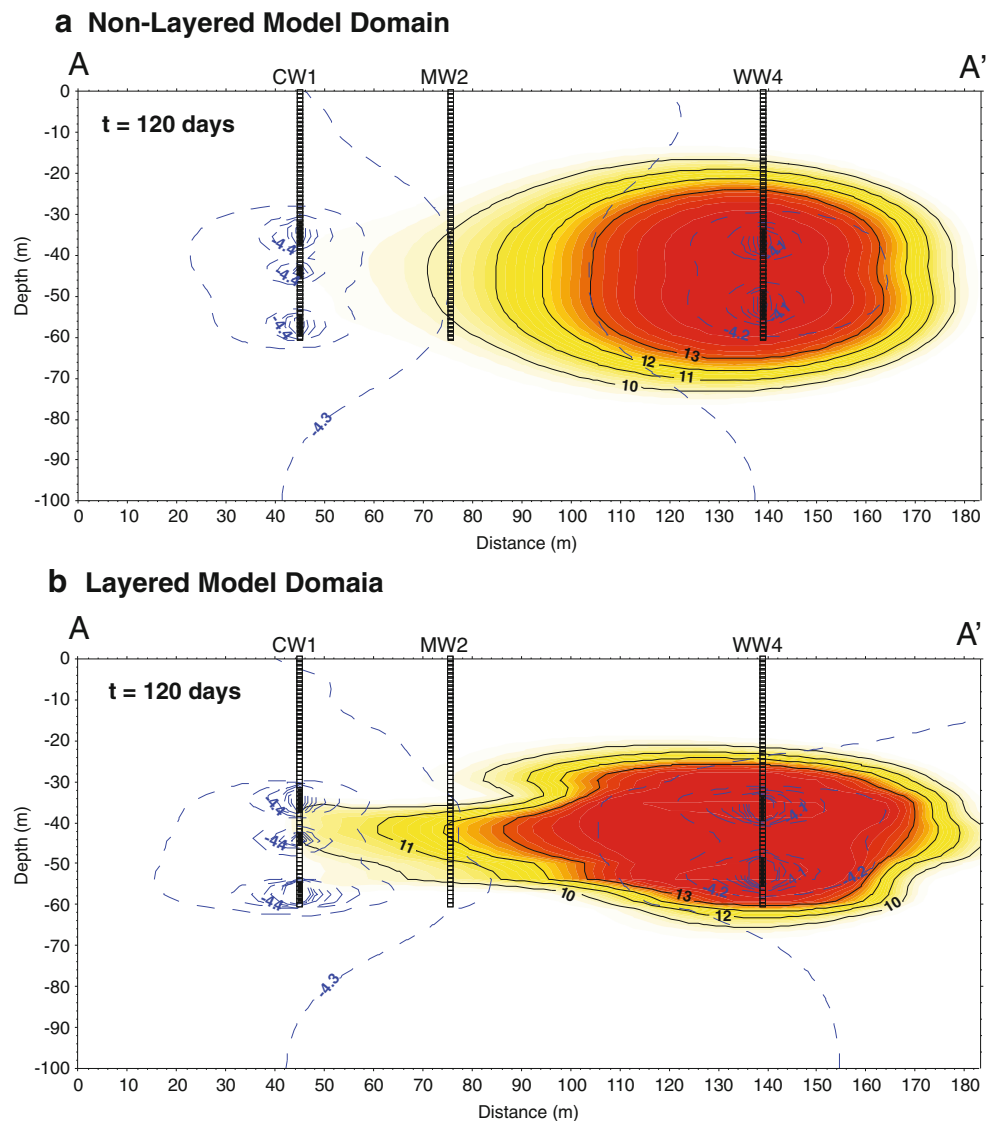
Fig. 8 Cross-section through the well field showing simulation results along cross-section A–A′ for the **a** non-layered and **b** layered model domains after a 120 day injection period at WW4. Contours for hydraulic head (m) (*blue dashed*) and temperature (°C) (*solid black*) are shown
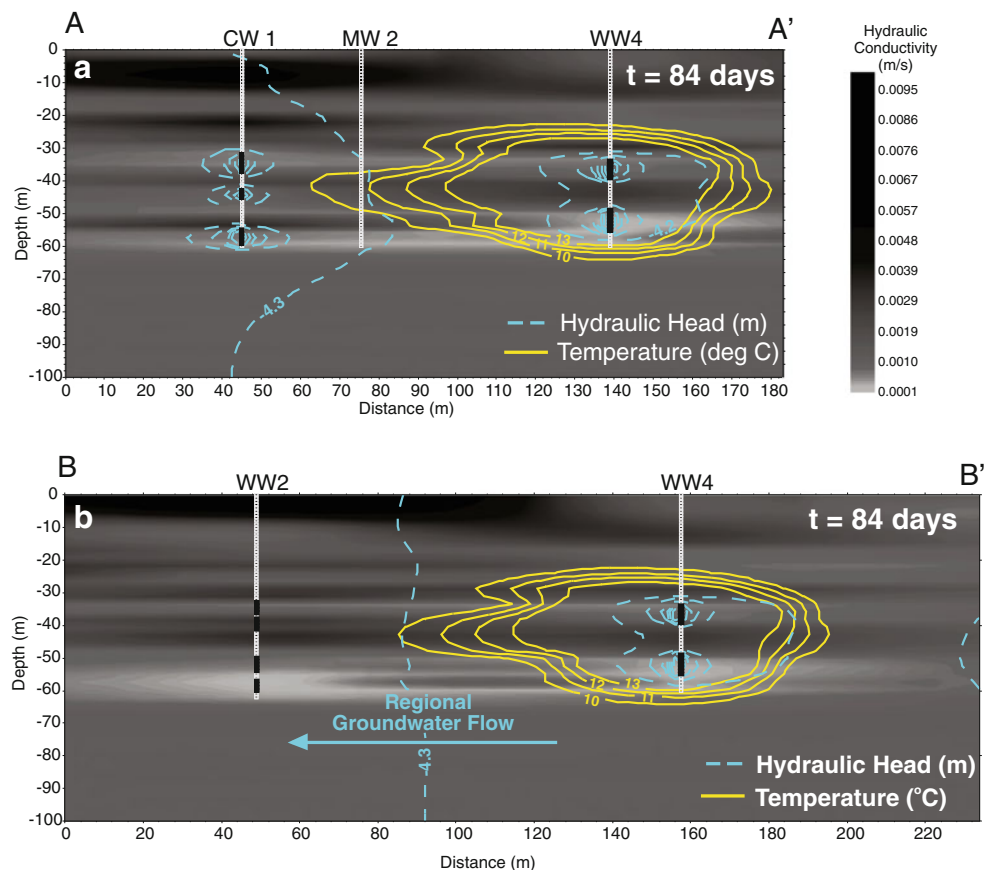
Fig. 9 Cross-sections **a** A–A′ and **b** B–B′ through the well field showing geological layering with corresponding hydraulic conductivity values and the hydraulic head (m) (*blue dashed line*) and temperature (°C) (*solid yellow*) distribution after 84 days of injection at WW4 (from Bridger and Allen 2010)

The temperature logging event that corresponds most closely to the simulated 84 days of injection at WW4 is July 7, 2001 (Fig. 10); observed and simulated temperatures are plotted for each of CW1, MW2 and WW4, which correspond to the wells shown in the cross-section in Fig. 9a. At CW1, the simulated and observed temperatures match closely, with only slight deviation at depths shallower than 30 m due to surface warming associated with the warm summer months. At MW2 virtually no thermal breakthrough is monitored; however, there is a very subtle positive increase in temperature near the base of the well. The simulated temperatures show evidence of breakthrough (~1 °C) between 35 and 50 m depth, but overall the simulation results are consistent with the observed temperature data. At the injection well, WW4, observed injection temperatures are isothermal down the well, whereas the simulation shows higher temperatures only within the screened intervals from 30 to 60 m where model boundary conditions were applied. The injection drop pipes in the production wells are positioned at the top of the well, several meters below the water table; thus, water mixes vertically down the borehole and can only exit the well at the screens.

Temperature logging results for the second cross-section (Fig. 9b) are not shown because WW2 had been used for injection during this period and temperatures had increased, so the simulation results with zero injection at WW2 are not represented in the actual data.

Figure 11 shows a similar cross-section through WW2, MW3 and CW3 after 120 days of injection at WW2. In this section, a higher permeability layer, located between the second and third well screens in WW2, appears to act as a preferential pathway for thermal plume movement; however, this layer pinches out before reaching the pumping well (CW3) and the thermal plume is retarded in the simulation (i.e., thermal breakthrough has not occurred after 120 days). The simulated temperatures in WW2 (injecting) show cooler temperatures above and below the well screens, suggesting that heat is not dispersing vertically near the borehole. Observed temperatures in the three wells are shown in Fig. 12. The observed temperatures in WW2 are constant throughout the injection zone as would be expected considering mixing in the water column. In MW3, observed temperatures show no evidence of warming; however, the simulation results suggest that some warming is taking place at 25–55 m depth. This simulated warming is related to the high permeability layer that extends from WW2 to MW3 in the model. Finally, at CW3, the simulation shows
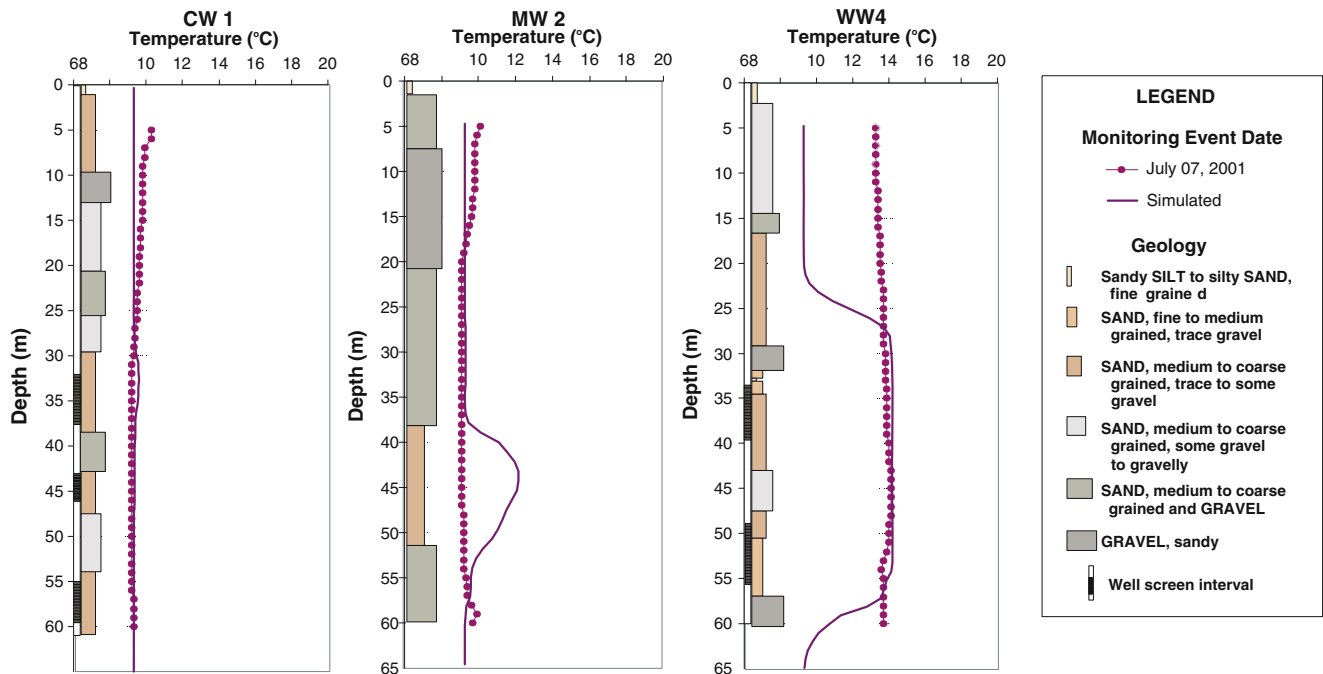
Fig. 10 Temperature logs collected in *CW1*, *MW2* and *WW4* on July 7, 2001 during injection at WW4 at the rate and temperature simulated in Fig. 9. Also shown is the geological layering and the well screen positions in the production wells

no evidence of warming, yet discrete high temperature spikes are observed at the various well screens, which suggests some breakthrough occurs. However, WW4 had been operating since April 2001, and it is likely that these temperature spikes are related to heat transport from WW4.

Storage of the heat was simulated using the layered and non-layered models for a period of 1 year (365 days) following 120 days of injection of 14 °C water at WW4. Figure 13 compares the simulated thermal plumes from both model domains after 30, 60, 120 and 365 days in cross-section through WW2 and WW4, oriented parallel to the regional flow direction. The results indicate that thermal storage is achieved (i.e., the plume has not dispersed entirely)

for up to 120 days in the layered domain despite preferential movement of the plume through higher permeability layers located above and below the top screen in WW4. In the non-layered case, the thermal plume maintains its overall shape but gradually shrinks in size as it drifts away from the well. After 60, 120 and 365 days, the centre of the plume has drifted approximately 16, 21 and 49 m from the well, respectively.

Figure 14 shows the simulated change in temperature over time in WW4 at depths of 37 m (middle of top screen), 44 m (between screens), and 52 m (middle of bottom screen) during the storage period for both model domains. For the layered model case, different rates of decreasing temperature are observed at each monitoring
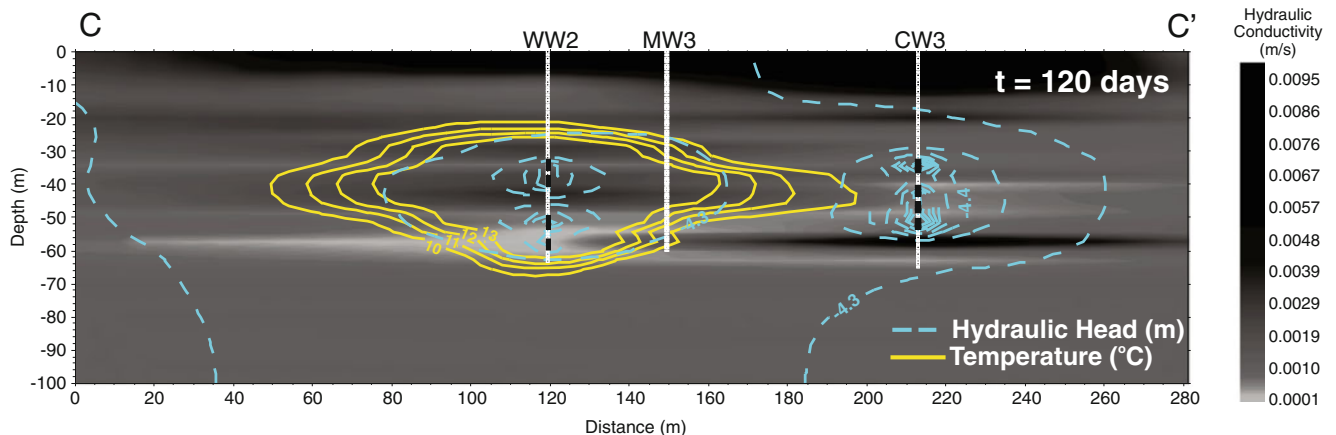

Fig. 11 Cross-section (*C–C′*) through the well field showing geological layering with corresponding hydraulic conductivity values and the hydraulic head (m) (*blue dashed line*) and temperature (°C) (*solid yellow*) distribution after 120 days of injection at *WW2*
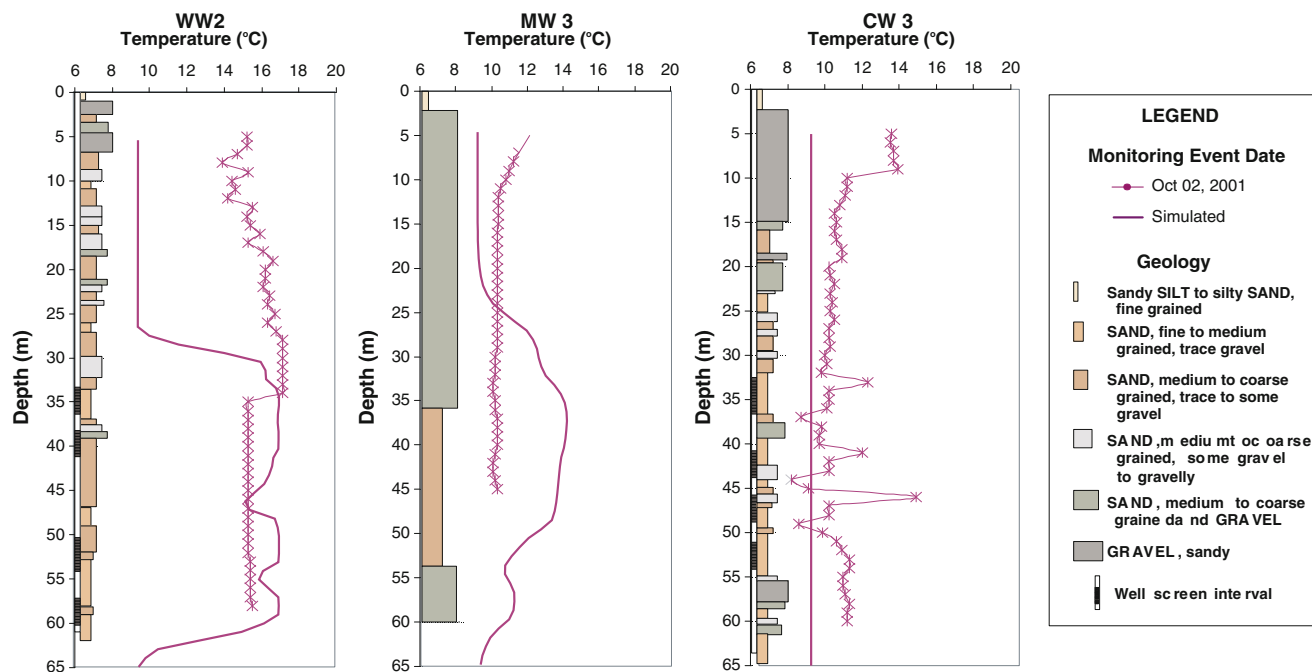
Fig. 12 Temperature logs collected in *WW2*, *MW3* and *CW3* on October 2, 2001 during injection at WW2 at the rate and temperature simulated in Fig. 11. Also shown is the geological layering and the well screen positions in the production wells

depth. This effect is attributable to the presence of layering and preferential movement of groundwater within higher permeability layers. Adjacent to the screens at 37 and 52 m depth, the permeability is lower, particularly adjacent to the lower screen (average $K=2.6\times10^{-4}$ m/s), and the thermal energy store is retained near the well. Between the screens at 44 m depth, the permeability is an order of magnitude higher (average $K=2.0\times10^{-3}$ m/s) and the thermal store is carried away rapidly by higher velocity groundwater flow. For the non-layered case, only small temperature differences are observed between the screens, reflecting the uniform aquifer conditions. It is important to note that the rate of temperature drop in the thermal store is reflective of both the aquifer conditions and the size of the thermal store (i.e., temperature declines would be more rapid for a smaller thermal plume and slower for a larger thermal plume).

Recovery of the thermal plume was evaluated both immediately following the injection (i.e., no storage period) in WW4 and WW2 and following 120 days of storage in WW4. Figure 15 compares the simulated thermal plume for the layered and non-layered models during extraction of heat at WW4 following 120 days of storage. In both cases, drift of the thermal plume away from the well has resulted in pumping of ambient groundwater on the opposite side of the well and a reduction in temperatures of extracted groundwater.

Figure 16 compares both the temperature of the extracted water from the layered and non-layered domains for instantaneous recovery (no storage) in WW4 and WW2, and for recovery from WW4 after 120 days of storage (as shown in Fig. 15). Comparison of recovered temperatures in WW4 and WW2 during instantaneous recovery generally indicates a similar response for both wells regardless of whether a layered or non-layered model was considered. It should be noted that the simulated temperature curve shown for WW2 represents an average temperature from the four well screens in this well. Unlike in WW4, where the recovery temperatures are similar for both screens, the recovery temperatures in the screens in WW2 differ by up to 1 °C. Although not shown, slightly higher recovery temperatures are observed in the second and third screen intervals versus the top and bottom screen intervals. The second and third screen intervals, however, do not correspond with the lower permeability layers in the well as might be expected (i.e., top and bottom screens have average K of 1.5×10^{-4} and 4.1×10^{-4} m/s versus 2.0×10^{-3} and 3.5×10^{-3} m/s in the second and third screens, respectively). Instead, it is inferred that this difference is a result of the middle screens being located closer to the main body of the plume, and also the geology at this location. As shown in Fig. 11, the gravel layers above and below the second screen receive heat preferentially in this well.

Comparison of the layered and non-layered cases for instantaneous recovery indicates that the recovered water in the layered model retains a slightly higher temperature. Also, storage efficiency, which was calculated by integrating the recovered heat over the extraction period and comparing this to the total injected heat, shows higher efficiencies in the layered cases (Fig. 16). This is most likely attributable to the presence of lower permeability layers at the screen intervals in the layered system, and improved thermal energy storage (or reduced advection of
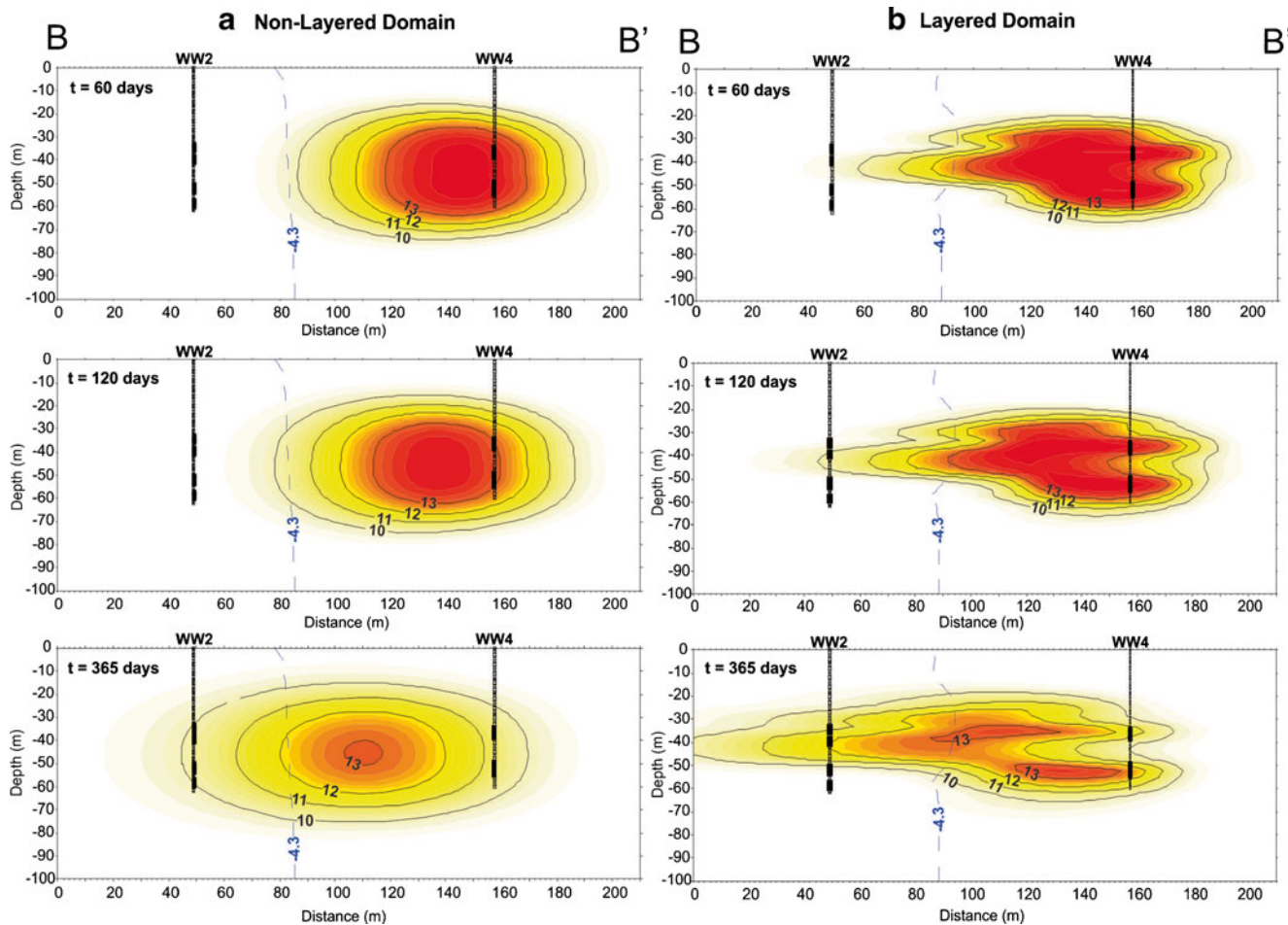
Fig. 13 Cross-sections (along *B–B′*) showing heat storage at WW4 after *60*, *120* and *365* days for **a** the non-layered domain and **b** the layered domain. Contours for hydraulic head (m) (*blue dashed*) and temperature (°C) (*solid black*) are shown
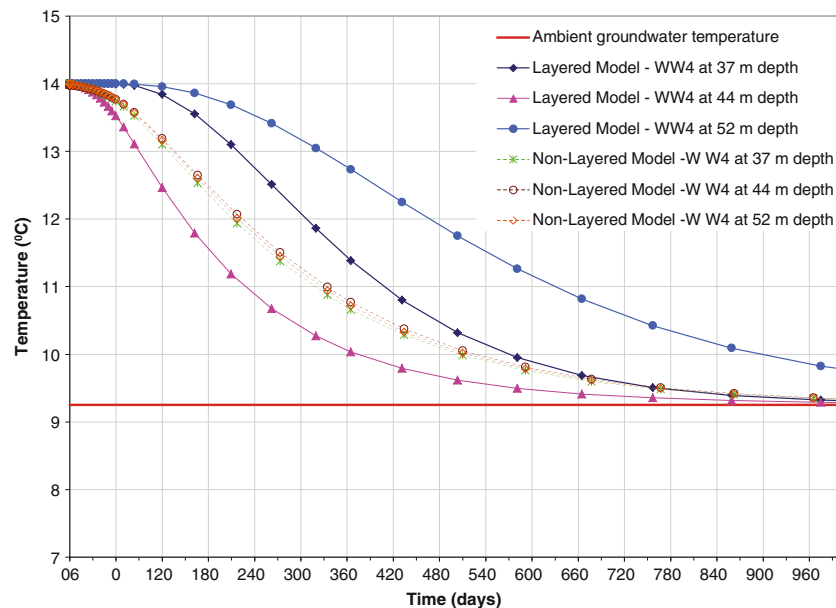

Fig. 14 Simulated temperature versus time during thermal storage in WW4 at three depths (37, 44 and 52 m) in the *layered* and *non-layered* model domains
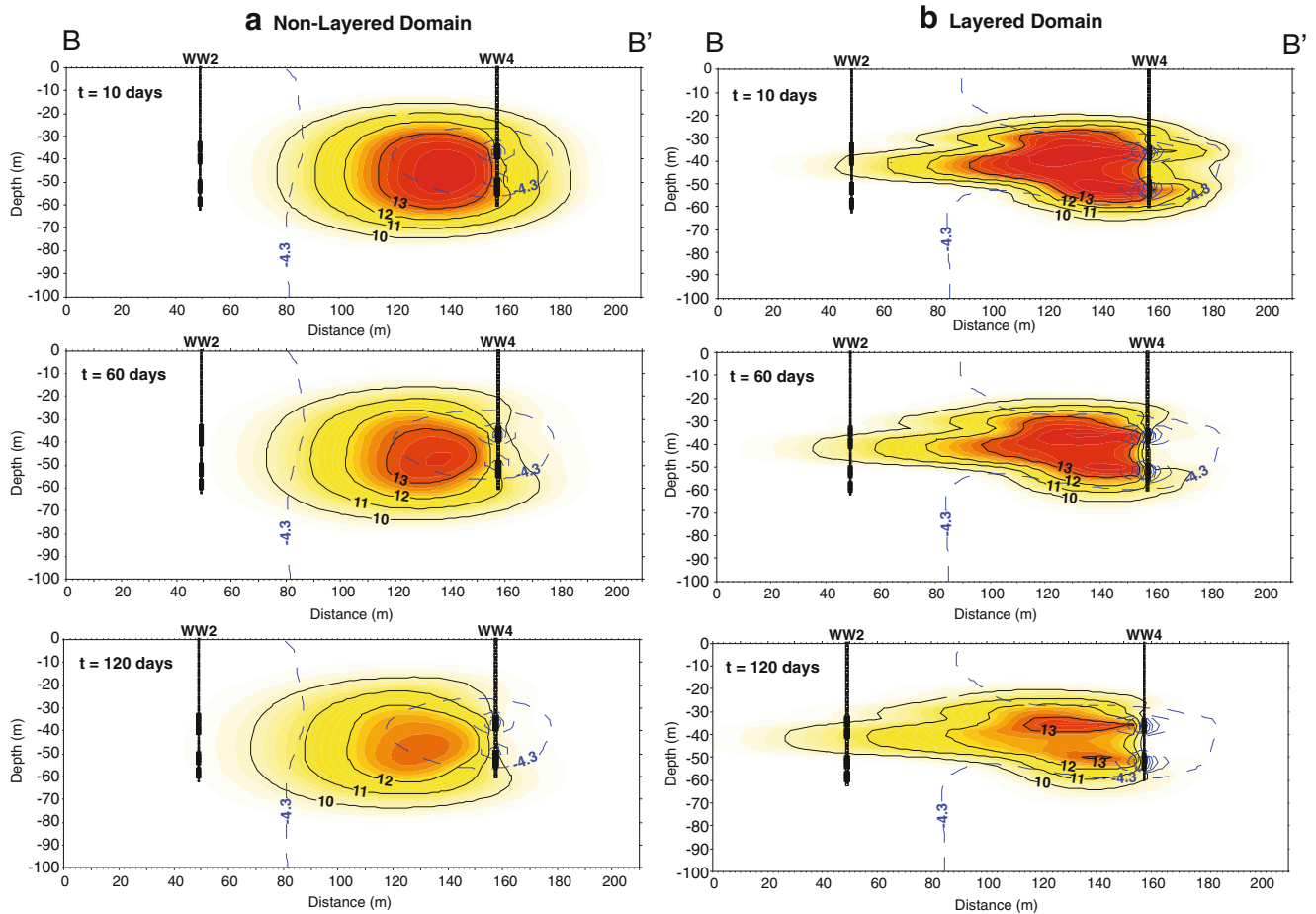
Fig. 15 Cross-sections (along *B–B′*) showing heat recovery at WW4 after *10*, *60* and *120* days following a 120 day storage period for **a** the non-layered domain and **b** the layered domain. Contours for hydraulic head (m) (*blue dashed*) and temperature (°C) (*solid black*) are shown
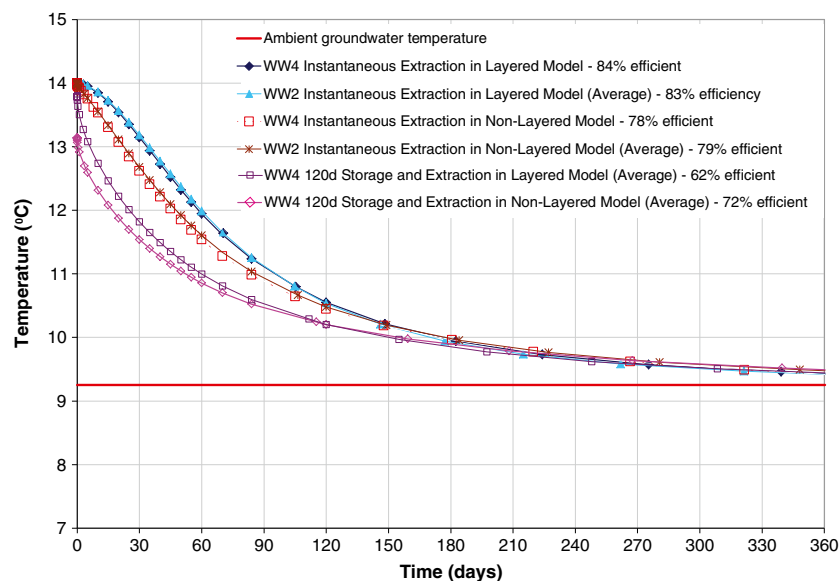

Fig. 16 Simulated temperature of extracted water versus time during thermal recovery in WW4 and WW2. Shown are the simulation results for instantaneous extraction and for storage and extraction in the layered and non-layered models and the calculated efficiencies for each case

the thermal plume) in these layers, as discussed previously in the storage section.

Finally, temperatures and efficiencies are lower for both the layered and non-layered models following 120 days of storage compared to the respective instantaneous recovery scenarios. Interestingly, the layered model shows a lower overall efficiency (62 %) compared to the non-layered case (72 %). This might suggest that heat drifts further away from the well in the layered model more quickly than in the non-layered model, possibly because the higher K units play a more important role at greater times. This effect is observed at 365 days during the storage cycle (Fig. 13).

Conclusions

Two flow and heat transport models were developed for the site; non-layered and layered. Overall, the results of transient flow calibration to the pumping test indicate that the incorporation of discrete layering in the layered model does not appear to provide any significant advantage for simulating hydraulic response of the aquifer to pumping. The low RMS errors also suggest that the level of flow calibration achieved is adequate.

A sensitivity analysis showed that, with the exception of vertical anisotropy and hydraulic gradient, the model is generally insensitive to changes in thermal and hydraulic parameters within the expected range for the site. The model is most sensitive to vertical anisotropy and hydraulic gradient.

The effects of geologic layering were evaluated by comparing simulation results from both the non-layered and layered model domains during the thermal energy injection, storage, and recovery phases of an ATES cycle. Visual comparison of heat plumes in the layered and non-layered models revealed that heat transport is largely controlled by the presence of higher permeability layers. In the layered model, the plume becomes more elongated with greater transport distances associated with higher permeability layers. Where thermal breakthrough does not occur after 120 days at the pumping well in the non-layered model, it does occur in the layered model. Overall, the simulation results for the layered model are generally consistent with the observed temperature data after 84 days of injection at WW4, and after 120 days at WW2 although in the latter case, the actual temperature logs for CW3 (which show temperature spikes at the screened depths) may reflect coincident operation of WW4.

Heat storage simulations demonstrated that while the thermal plume became distorted and elongated in the layered system, the plume remained intact and did not fully disperse down gradient; the plume in the non-layered case retained its shape. For the layered model case, temperatures decreased at different rates at the monitoring depths in the injection well, whereby zones with lower K remained at higher temperature compared to the more permeable zones. For the non-layered case, only small temperature differences were observed between the screens, reflecting the uniform aquifer conditions.

Recovery was evaluated both immediately following the injection (i.e., no storage period) in WW4 and WW2 and following 120 days of storage in WW4. Recovered temperatures in WW4 and WW2 during instantaneous recovery are similar for both wells regardless of whether a layered or non-layered model was considered; however, the recovered water in the layered model retains a slightly higher temperature. Short-term storage efficiency is higher for the layered cases, which is likely related to the presence of lower permeability layers at the screen intervals in the layered system. The storage efficiency is lower for the both the layered and non-layered models following 120 days of storage compared to the respective instantaneous recovery scenarios. The lower overall long-term storage efficiency of the layered model (62 %) compared to the non-layered case (72 %) is an interesting result and may reflect a more dominant role that the high K layers play at larger times.

The slight differences between the observed and simulated temperatures (for the injection cases) are likely related to a number of factors. Simulated and observed borehole temperatures reflect a combination of screen placement, apportionment of flow rates, means of injection (drop pipe), vertical mixing in the borehole, and geological layering. The actual wells were screened over the less permeable sediments in order to avoid potential short-circuiting that might occur in the gravel layers. However, the observed temperature data suggest that thermal short-circuiting did occur at some wells. Generally, the simulations showed somewhat earlier breakthrough compared to what was observed and this is most likely related to lateral continuity of the high permeability gravel layers in the model. The layering was represented as most possible using the available well data. However, poor quality lithology logs at the three monitoring wells between the production wells (see Fig. 2) precluded the development of a better-constrained layered system. As mentioned earlier, the hydraulic conductivities were interpolated from the production well data, using a few control points outside of the well field to allow the layers to extend laterally through the domain. Thus, there is uncertainty as to how representative these model layers are. Nevertheless, the approach used to generate the layered system, using available grain-size data and computer-assisted interpolation, provided a means for representing heterogeneity in the model, and this representation was important for obtaining simulation results that best represented the observations at the site.

References

Akindunni FF, Gillham RW (1992) Unsaturated and saturated flow in response to pumping of an unconfined aquifer: numerical investigation of delayed drainage. Ground Water 30(6):873–884

Anderson MP, Woessner WW (1992) Applied groundwater modeling: simulation of flow and advective transport. Academic, San Diego, CA, 381 pp

Andersson O (2007) Aquifer thermal energy storage. In: Paksoy HO (ed) Thermal energy storage for sustainable energy consumption. The Netherlands, Dordrecht, Springer, pp 155–176

Baker FG, Pavlik HF (1990) Characterization and modelling of groundwater flow in a heterogeneous aquifer system to evaluate contaminant migration. In: Bachu S (ed) Fifth Canadian/American conference on hydrogeology. National Water Well Association, Westerville, OH

Bartels J, Kabus F (2003) Seasonal aquifer solar heat storage at Rostock-Brinckmanshoe: first operational experience and aquifer simulation. In: Proceedings of Futurestock, 9th International Conference on Thermal Energy Storage. Warsaw, Poland

Bridger DW (2006) Influence of aquifer heterogeneity on the design and modelling of aquifer thermal energy storage (ATES) systems. MSc Thesis, Simon Fraser University, Canada, 193 pp

Bridger DW, Allen DM (2005) Designing aquifer thermal energy storage systems. ASHRAE J 47(9):S32–S38

Bridger DW, Allen DM (2010) Heat transport simulations in a heterogeneous aquifer used for aquifer thermal energy storage (ATES). Can Geotech J 47(1):96–115. doi:10.1139/T09-078

Busheck TA, Doughty C, Tsang CF (1983) Prediction and analysis of a field experiment on a multilayered aquifer thermal energy storage system with strong buoyancy flow. Water Resour Res 19(5):1307–1315

Davis SN (1969) Porosity and permeabiliy of natural materials. In: De Wiest RJM (ed) Flow through porous media. Academic, New York, pp 54–89

Domenico PA (1972) Concepts and models in groundwater hydrology. McGraw-Hill, New York, 405 pp

Eggen G, Vangsnes G (2005) Heat pump for district cooling and heating at Oslo airport, Gardermoen. In: Proceedings of the 8th IEA Heat Pump Conference. Las Vegas, NV, November, May 30–June 2, 2005

Fofonoff P, Millard RC Jr (1983) Algorithms for computation of fundamental properties of seawater. UNESCO Tech Papers Mar Sci 44, UNESCO, Paris, 53 pp

Freeze RA, Cherry JA (1979) Groundwater. Prentice Hall, Englewood Cliffs, NJ

Hall SJ, Raymond JR (1992) Geohydrologic characterization for aquifer thermal energy storage. In: Proceedings of the Intersociety Energy Conversion Engineering Conference. San Diego, CA, August, 1992, pp 75–81

Hazen A (1893) Some physical properties of sands and gravels. 24th annual report, Massachusetts State Board of Health, Boston

Hellstrom G, Sanner K (2000) EED-Earth energy designer user manual, version 2. EED, Lahnau, Germany

Hidalgo JJ, Carrera J, Dentz M (2009) Steady state heat transport in 3D heterogeneous porous media. Adv Water Resour 32(8):1206–1212. doi:10.1016/j.advwatres.2009.04.003

IF Technology (1995) Underground thermal energy storage: state of the art 1994. IF Technology, Arnhem, The Netherlands

Johnson AI (1967) Specific yield: compilation of specific yields for various materials. US Geol Surv Water Suppl Pap 1662-D

Jumikis AR (1962) Soil mechanics. Van Norstrand, New York, 384 pp

Kim J, Lee Y, Yoon WS, Jeon JS, Koo MH, Keehm Y (2010) Numerical modeling of aquifer thermal energy storage system. Energy 35(12):4955–4965. doi:10.1016/j.energy.2010.08.029

Lee KS (2011) Numerical simulation on the continuous operation of an aquifer thermal energy storage system under regional groundwater flow. Energy Sources Part A: Recover Utilization Environ Eff 33(11):1018–1027. doi:10.1080/15567030903330744

Lee KS (2010) A review on concepts, applications, and models of aquifer thermal energy storage systems. Energies 3:1320–1334. doi:10.3390/en3061320

Lo Russo S, Vincenzo Civita M (2009) Open-loop groundwater heat pumps development for large buildings: a case study. Geothermics 38:335–345

Marx R, Nussbicker-Lux J, Bauer D, Heidemann W, Druck H (2011) Seasonal thermal energy stores: design, operation and applications. Chem Ing Tech 83(11):1994–2001. doi:10.1002/cite.201100064

Maynard S (2006) Ground source heat pumps: pros, cons, and experiences. In: Abstracts, Banff Pork Seminar, January 17–20, 2006. Banff, AB, Canada. http://www.banffpork.ca. Accessed January 2006

Moench AF, Garabedian SF, LeBlanc DR (2001) Estimation of hydraulic parameters from an unconfined aquifer test conducted in a glacial outwash deposit, Cape Cod Massachusetts, US Geol Surv Prof Pap 1629

Molz FJ, Melville JG, Parr AD, King AD, Hoff MT (1983a) Aquifer thermal energy storage: a well doublet experiment at increased temperatures. Water Resour Res 19(1):149–160

Molz FJ, Melville JG, Guven O, Parr AD (1983b) Aquifer thermal energy storage: an attempt to counter free thermal convection. Water Resour Res 19(4):922–930

Morris DA, Johnson AI (1967) Summary of hydrologic and physical properties of rock and soil materials, as analysed by the Hydrologic Laboratories of the U.S. Geological Survey 1948–1960. US Geol Surv Water Suppl Pap 1839-D, 42 pp

Paksoy HO, Andersson O, Abaci S, Evliya H, Turgot B (2000) Heating and cooling of a hospital using solar energy coupled with seasonal thermal energy storage in an aquifer. Renewable Energy 19:117–122

Palmer CD, Blowes DW, Frind EO, Molson JW (1992) Thermal energy storage in an unconfined aquifer: 1. field injection experiment. Water Resour Res 28(10):2845–2856

Rehm BW, Groenewold GH, Morin KA (1980) Hydraulic properties of coal and related materials, Northern Great Plains. Ground Water 18(6):551–561

Tsang CF, Busheck T, Doughty C (1981) Aquifer thermal energy storage: a numerical simulation of Auburn University field experiments. Water Resour Res 17(3):647–658

Vail WL, Jenne EV (1994) Optimizing the design and operation of ATES systems. In: Proceedings of the International Symposium on Aquifer Thermal Energy Storage. Tuscaloosa, AL, November 1994, pp 9–13

Vanhoudt D, Desmedt J, Van Bael J, Robeyn N, Hoes H (2011) An aquifer thermal storage system in a Belgian hospital: long-term experimental evaluation of energy and cost savings. Energy Build 43(12):3657–3665. doi:10.1016/j.enbuild.2011.09.040

WASY (2005) FEFLOW 5.2. Finite element subsurface flow & transport simulation system. WASY, Berlin, Germany

Witte HJL, van Gelder GJ, Spitler JD (2002) In situ measurement of ground thermal conductivity: the Dutch perspective. ASHRAE Transact 108(1):263–272

Xue Y, Xie C, Li Q (1990) Aquifer thermal energy storage: a numerical simulation of field experiments in China. Water Resour Res 26(10):2365–2375